

Hierarchical porous carbon nanofibers with ultrasmall-sized cobalt disulfide/tungsten disulfide hybrid composites for high-rate lithium storage kinetics

Dong-Yo Shin^a, Jung Soo Lee^b, Hyo-Jin Ahn^{a,b,*}

^a Program of Materials Science & Engineering, Convergence Institute of Biomedical Engineering and Biomaterials, Seoul National University of Science and Technology, Seoul 01811, Republic of Korea

^b Department of Materials Science and Engineering, Seoul National University of Science and Technology, Seoul 01811, Republic of Korea

ARTICLE INFO

Keywords:

Cobalt disulfide
Tungsten disulfide
Micropores
Mesopores
Ultrafast lithium ion batteries

ABSTRACT

Recently, transition metal dichalcogenides (TMDs) have attracted considerable attention as anode materials in ultrafast lithium ion batteries because of their high theoretical capacity and outstanding ion diffusion kinetics. Despite these remarkable properties, TMDs exhibit fast capacity fading and insufficient Li storage kinetics, owing to the excessive volume expansion and low electric/ionic transfer rate.

The aim of this study is to reinforce the structural stability and Li storage kinetics of TMDs through the use of well-dispersed CoS₂ and WS₂ ultrasmall particles (USPs) embedded in hierarchical porous carbon nanofibers, including micro/mesoporous composite structures. As expected, this architecture offers a high specific capacity (718.0 mAh g⁻¹) with the capacity retention of 93.4% after 100 cycles at 0.1 A g⁻¹ owing to increased Li storage sites and prevention of volume expansion of CoS₂ and WS₂ USPs. In particular, a remarkable fast discharge capacity (444.5 mAh g⁻¹) with the capacity retention of 90.2% after 1000 cycles are noted. These results are related to the high number of Li ion storage sites, effective prevention of volume expansion of well-dispersed CoS₂ and WS₂ USPs, short Li ion diffusion length, and favorable Li ion acceptability, which is caused by the hierarchical porous structure containing meso/micropores.

1. Introduction

Recently, with advancements of high-performance electronic devices such as electrical vehicles, military drones, and robot suits, research has been conducted on improving their energy storage properties (e.g., energy density, power density, charging speed, lifetime, and safety) [1,2]. In accordance with the electronic industry trends, lithium ion batteries (LIBs) have become the predominant energy source, because of their high volumetric/gravimetric energy density and long lifetime [3]. However, LIBs still face critical problems related to insufficient energy density, poor lifetime, and long charging time, and thus cannot be used in high-performance electronic devices. Regarding these various efforts have been made to establish anode materials, involving metal oxides and metal chalcogenides [4–6].

Transition metal dichalcogenides (TMDs) with MX₂ structures, such as CoS₂, WS₂, MoS₂, and FeS₂, are promising candidates as anode materials because of their remarkable theoretical capacity, which is caused

by utilizing all oxidation states with conversion reactions [7–12]. Among the TMD materials, CoS₂ has been used in various energy storage devices such as LIBs, sodium ion batteries, supercapacitors, and lithium–air batteries, owing to its excellent physical, chemical, and electrochemical characteristics [13]. In particular, CoS₂ is useful as an anode material in LIBs because of its high theoretical capacity (870 mAh g⁻¹). However, the fast capacity fading and poor Li storage kinetics of CoS₂, which occur due to large volume expansion and low electrical conductivity, hinder its applications in ultrafast LIBs [13]. Although WS₂ has a relatively lower theoretical capacity (432 mAh g⁻¹) than those of other TMD materials, it exhibits outstanding Li storage kinetics due to its two-dimensional crystal structure [14]. WS₂ has a typical 2D layered structure and a large interlayer distance of ~ 0.62 nm compared to the interlayer distance of graphite (~0.34 nm), which favours Li ion diffusion in the WS₂ structure [14]. However, WS₂ exhibits low cycling stability and insufficient ion diffusion rate due to large volume expansion, low structural stability, and poor electrical conductivity; its use as an

* Corresponding author at: Department of Materials Science and Engineering, Seoul National University of Science and Technology, Seoul 01811, Republic of Korea
E-mail address: hjahn@seoultech.ac.kr (H.-J. Ahn).

anode material for ultrafast LIBs is challenging. To solve these problems, new composite structures on the complexation of well-dispersed TMDs in hierarchical porous carbon, including mesopores and micropores, must be designed.

Herein, to improve the cycling stability and Li storage kinetics, we prepared an architecture of well-dispersed CoS₂ and WS₂ ultrasmall particles (USPs) embedded in porous carbon nanofibers (PCNFs) comprising microporous and mesoporous composite structures. For this purpose, electrospinning, polymer decomposition, and sulfurization were used. The developed architecture exhibits improved specific capacity and cycling stability owing to the synergistic effect of CoS₂ and WS₂ USPs with carbon, which results in the effective prevention of volume expansion by carbon composites and an increase in the number of Li storage sites. Furthermore, to enhance the high-rate charge/discharge performance, the hierarchical porous structure of PCNFs was modified using polyvinylpyrrolidone (PVP) and poly(methyl methacrylate) (PMMA) polymers with different intrinsic properties. According to the ion diffusion behaviour in the porous structure, the micropores and mesopores can effectively provide favourable ion acceptability and short Li ion diffusion length by high specific surface area during ultrafast cycling. As expected, this architecture exhibits excellent specific capacity, outstanding cycling stability, and remarkable high-rate charge/discharge performance, resulting from the high number of Li storage sites, prevention of volumetric expansion, and favourable Li ion acceptability.

2. Experiments

2.1. Chemicals

Cobalt phthalocyanine (C₃₂H₁₆CoN₈, 97%), tungsten chloride (WCl₄, 99.9%), oleylamine (C₁₈H₃₇N, 70%), ethyl alcohol (C₂H₆O, 99.5%), oleic acid (C₁₈H₃₄O₂, 90%), polyvinylpyrrolidone (PVP, M_w = 360,000), poly(methyl methacrylate) (PMMA, M_w = 120,000), polyacrylonitrile (PAN, M_w = 150,000), N,N-dimethylformamide (DMF, 99.8%), sulfur (S, 99%), cobalt sulfide (CoS₂, 99.98%), and tungsten sulfide (WS₂, 99%) were purchased from Sigma Aldrich. Methanol (CH₄O, 99.8%) and acetone (CH₃COCH₃, 99.7%) were purchased from SAMCHUN. All chemicals and reagents were used without purification process.

2.2. Synthesis of CoS₂/WS₂ USPs embedded in micro/meso PCNFs

CoS₂/WS₂ USPs, embedded in PCNFs comprising of micropores and mesopores, were synthesized using electrospinning, polymer decomposition, and sulfurization. The synthesis method for WO₃ is described in detail in the [Supporting Information](#). First, 3 wt% WO₃ USPs, 3 wt% C₃₂H₁₆CoN₈, and 8 wt% PAN were dissolved in DMF. Then, 6 wt% PVP and 6 wt% PMMA, used as pore-forming agents of micropores and mesopores, respectively, were added to the prepared solution. For the electrospinning process, the mixed solution was transferred to a syringe equipped with a 23-gauge needle. The applied feed rate and voltage were 0.04 ml h⁻¹ and 15 kV, respectively. The humidity was maintained at 5%. Thereafter, S powder was added at a 2:1 M ratio to the as-spun nanofibers and placed 1.0 cm below the as-spun nanofibers on the mesh in a crucible for sulfurization. The as-spun nanofibers were stabilized and carbonized at 230 °C for 2 h in air and at 800 °C for 2 h in a high-purity N₂ atmosphere. The CoS₂ and WS₂ USPs embedded in hierarchical PCNFs are hereinafter referred to as CoS₂/WS₂-HPCNFs. For comparison, bare CNFs fabricated using only PAN without any other agents (referred to as conventional CNFs), CoS₂/WS₂ embedded in CNFs without PMMA and PVP (referred to as CoS₂/WS₂-CNFs), and CoS₂/WS₂ embedded in microporous CNFs without PMMA (referred to as CoS₂/WS₂-PCNFs) were prepared.

2.3. Characterization

The structures and morphologies of all samples were investigated using field-emission scanning electron microscopy (FESEM, Hitachi S-4800) and transmission electron microscopy (MULTI/TEM; Tecnai G², KBSI Gwangju Center), and energy-dispersive X-ray spectroscopy (EDS). The porosities and pore structures were analyzed using Brunauer–Emmett–Teller (BET) and Barrett–Joyner–Halenda (BJH) plots. The crystal structures and chemical states were examined via X-ray diffraction (XRD, EMPyrean, Panalytical) in the 2θ range of 10° to 90° using Cu Kα radiation and X-ray photoelectron spectroscopy (XPS, K-ALPHA+, Thermo Scientific) using Al Kα radiation. A differential scanning calorimetry (DSC) analysis of the PAN/PMMA/PVP nanofibers was performed in the temperature range of 25–600 °C under N₂ atmosphere.

2.4. Electrochemical characterization

To investigate the electrochemical performance of the prepared samples, a mixed slurry comprising of 80 wt% samples, 10 wt% ketjen black, and 10 wt% polyvinylidene fluoride in NMP solvent was coated onto a Cu foil (thickness of 18 μm) and dried at 100 °C for 9 h. The densities of all electrodes were optimized to 11.7 ± 0.1 mg cm⁻². Then, in an Ar-filled glove box with H₂O and O₂ contents of <5 ppm, a coin-type cell was manufactured using Li metal (Honjo Chemical, 99.999%) as the cathode, a porous polypropylene membrane (Celgrad 2400) as a separator, and prepared electrodes in 1.2 M LiPF₆ with ethylene carbonate and dimethyl carbonate (7:3) as the electrolyte. Electrochemical impedance spectroscopy (EIS, Autolab, Metrohm) measurements were recorded in the frequency range of 10² kHz to 10⁻² Hz at 5 mV using an AC signal to confirm the electrochemical kinetics and electrochemical resistance. The cycling performances of all samples were measured at 0.05–3.0 V (vs. Li/Li⁺) using a battery cycler (WMPG 3000S, WonATech Corp.). The cycling stabilities were investigated at 0.1 A g⁻¹ over 100 cycles. The rate capabilities were measured at current densities of 0.1, 0.3, 0.7, 1.0, 1.5, 2.0, and 3.0 A g⁻¹. The long-term tests of all samples were conducted at a current density of 3.0 A g⁻¹ over 1000 cycles.

3. Results and discussion

Fig. 1 shows a schematic illustration of the preparation of CoS₂ and WS₂ USPs in PCNFs with micropores and mesopores. The Co and WO₃ embedded in the as-spun nanofibers containing PAN, PVP, and PMMA polymers were fabricated using electrospinning. In a mixed solution of several polymers, each polymer undergoes phase separation depending on its viscosity and molecular weight [15,16]. The PMMA polymer with high viscosity was located to an aggregated state in the PAN matrix, whereas, the PVP polymer was evenly distributed in the PAN matrix due to its similar viscosity to that of the PAN polymer (**Fig. 1a**). Based on the phase separation caused by the inherent properties of the polymers, the dispersed polymer in the PAN matrix can lead to the creation of various types of pores during polymer decomposition and removal. During carbonization and sulfurization, the PMMA and PVP polymers decomposed at temperatures of >320 °C and >450 °C, respectively (**Fig. 1b** and **Fig. S1**). Depending on the phase separation and distribution of the PMMA and PVP polymers, hierarchical porous structures including mesopores (2–50 nm) and micropores (<2 nm), are formed by the decomposition of PMMA and PVP, respectively. As a result, the CoS₂/WS₂-CNFs (prepared without PMMA and PVP polymers) indicated a dense CNF structure with low porosity. The CoS₂/WS₂-PCNF (prepared with addition of PVP polymer) indicated a microporous structure with a small separated PVP polymer. On the other hand, CoS₂/WS₂-HPCNF (prepared with addition of PMMA and PVP polymers) indicated a hierarchical meso/microporous structure by largely agglomerated PMMA with separated PVP polymers in the PAN matrix. The micropores and mesopores can improve the accessibility of the electrolyte and reduce

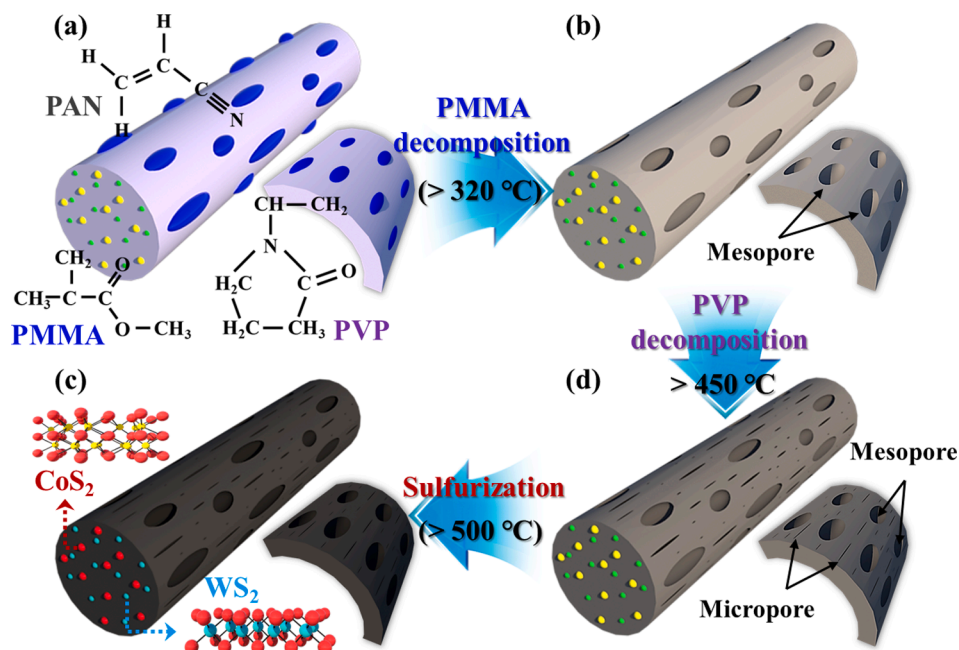
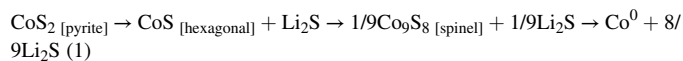


Fig. 1. Schematic illustration of formation steps of meso/micro pores with well-dispersed CoS_2 and WS_2 USPs in PCNFs.

the Li ion diffusion length, respectively, resulting in an increased rate capability. Then, the sulfurization reactions of Co ($\text{Co} + 2\text{S} \rightarrow \text{CoS}_2$) and WO_3 ($2\text{WO}_3 + 7\text{S} \rightarrow 2\text{WS}_2 + 3\text{SO}_2$) occurred due to the reaction of metal and sulfur, resulting from the sulfurization atmosphere by thermal evaporation of the S powder at temperatures of $>500\text{ }^{\circ}\text{C}$ (Fig. 1d and Fig. S2). Notably, the use of CoS_2 can result in a high specific capacity owing to its outstanding theoretical capacity ($\sim 871\text{ mAh g}^{-1}$) because CoS_2 can store 4 M Li^+ per 1 M CoS_2 . [13]. In general, the Li storage mechanism of CoS_2 is expressed, as follows [17]:



CoS_2 undergoes a phase transition with a complex sequential reaction from pyrite to the hexagonal phase upon Li intercalation, which induces a high irreversible conversion reaction and large volume change of CoS_2 . Whereas, WS_2 can lead to a high rate capability owing to the high ion diffusion rate resulting from the large interlayer spacing ($\sim 0.62\text{ nm}$) [14]. As a result, well-dispersed CoS_2 and WS_2 USPs in

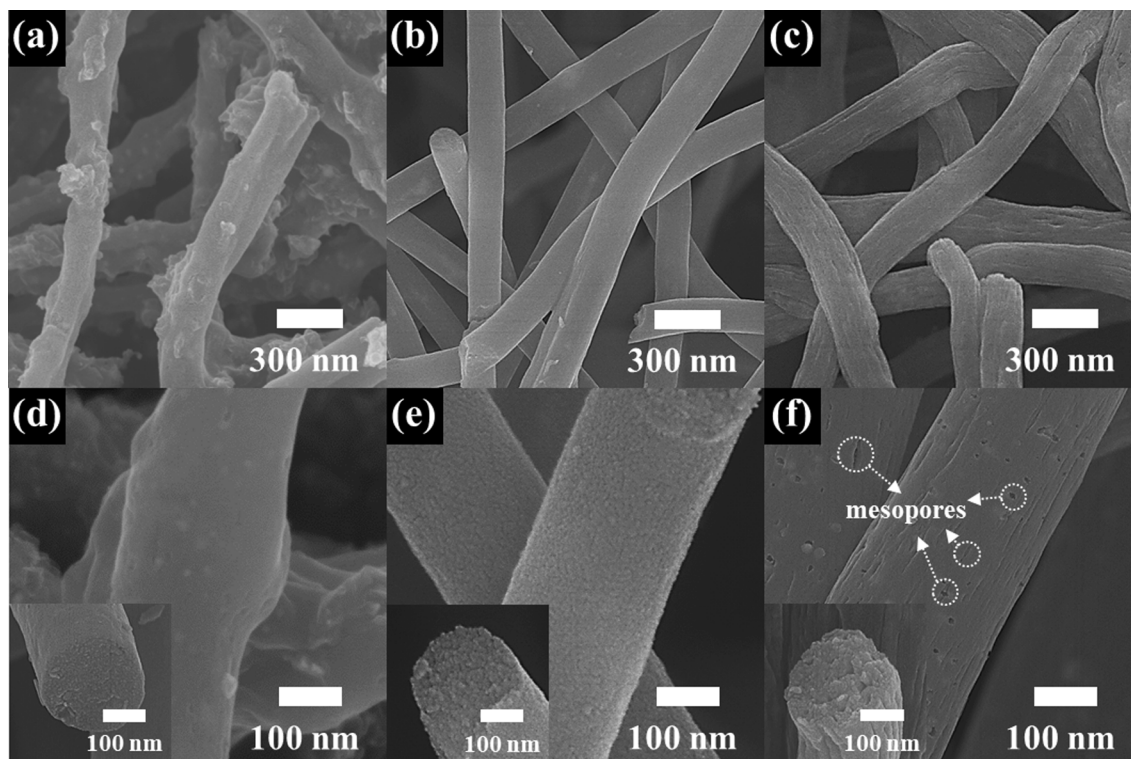


Fig. 2. (a-c) Low- and (d-f) high-magnification FESEM images of CoS_2/WS_2 -CNF, CoS_2/WS_2 -PCNF, and CoS_2/WS_2 -HPCNF, respectively.

PCNFs with micropores and mesopores can realize excellent high-rate charge/discharge performance by Li ion storage kinetics.

Fig. 2 displays low-magnification (Fig. 2a–c) and high-magnification (Fig. 2d–f) FESEM images of the CoS₂/WS₂-CNF, CoS₂/WS₂-PCNF, and CoS₂/WS₂-HPCNF, respectively. As shown, all samples have a network-like structure, which can provide an effective electron transfer during cycling performance. The CoS₂/WS₂-CNF indicated a smooth surface with a diameter of 266.7–285.9 nm (Fig. 2a, 2d). In contrast, the CoS₂/WS₂-PCNF (Fig. 2b, 2e) and CoS₂/WS₂-HPCNF (Fig. 2c, 2f) showed rough surfaces with diameters of 242.9–265.7 and 249.2–268.6 nm, respectively. The nanofiber morphologies of the CoS₂/WS₂-PCNF and CoS₂/WS₂-HPCNF were more uniform than that of the CoS₂/WS₂-CNF, because CoS₂ and WS₂ USPs were well dispersed in the PCNFs, resulting from the repulsion force by the polymer chains of PVP and PMMA (Fig. S3) [18]. Furthermore, mesopores were observed on the rough CoS₂/WS₂-HPCNF surface compared with the other samples due to the hierarchical porous structure. This structure including micropores and mesopores provides a short Li diffusion length and fast ion acceptability, which can improve the high-rate charge/discharge performance.

To further demonstrate the composite structure of the CoS₂/WS₂-HPCNF, the TEM and TEM-EDS mapping results were analyzed. The CoS₂/WS₂-HPCNF showed well-dispersed CoS₂ and WS₂ USPs in the PCNFs (Fig. 3a). The USP sizes of CoS₂ and WS₂ were 7.2–11.3 and 4.1–6.5 nm, respectively (Fig. 3b). Furthermore, the interlayer spacings of 2.52 Å, corresponding to the (210) plane of CoS₂, and 6.20 Å, corresponding to the (002) plane of WS₂, were clearly observed, as shown in Fig. 3c and 3d [13,19]. These results are in agreement with the selected area electron diffraction (SAED) patterns of the CoS₂/WS₂-HPCNF, and confirming that mesopores (scale of 2–50 nm) were well-formed on the surface (Fig. S4) [13,20]. According to the TEM-EDS mapping results (Fig. 3e), all elements (C, O, Co, W, and S) were uniformly dispersed, indicating that CoS₂ and WS₂ USPs were embedded in the PCNFs.

Fig. 4a shows the BET results of all samples measured by the adsorption/desorption isotherms of N₂. The isotherms of the CoS₂/WS₂-CNF and CoS₂/WS₂-PCNF exhibit type-I curves, implying a microporous structure (pore size of <2 nm), as per the definition provided by the

International Union of Pure and Applied Chemistry [21]. In contrast, the isotherm of the CoS₂/WS₂-HPCNF shows a type-IV curve, signifying a mesoporous structure (pore size of 2–50 nm). Furthermore, the specific capacity and total pore volume of all samples were 320.8 m² g⁻¹ and 0.14 cm³ g⁻¹ for the CoS₂/WS₂-CNF, 440.5 m² g⁻¹ and 0.20 cm³ g⁻¹ for the CoS₂/WS₂-PCNF, and 545.7 m² g⁻¹ and 0.27 cm³ g⁻¹ for the CoS₂/WS₂-HPCNF (Fig. 4b). In particular, the specific surface areas of the CoS₂/WS₂-PCNF and CoS₂/WS₂-HPCNF were 1.4 and 1.7 times higher than that of the CoS₂/WS₂-CNF, respectively. These results indicate that the micropores and mesopores were clearly formed by the thermal decomposition of PVP and PMMA during sulfurization (Fig. 4c). In addition, according to the BJH data of all samples (Fig. 4d), the mesopore volume and distribution in the CoS₂/WS₂-HPCNF with sizes of 10–30 nm were higher than those in the CoS₂/WS₂-CNF and CoS₂/WS₂-PCNF. The mesopore volume fraction of the CoS₂/WS₂-HPCNF (38.7%) was higher than those of the CoS₂/WS₂-CNF (5.5%) and CoS₂/WS₂-PCNF (10.0%) due to the formation of mesopores by the thermal decomposition of the PMMA polymer. Detailed BET results (specific surface area, total pore volume, average pore diameter, and pore volume fraction) are listed in Table S1. The increased mesopore volume and specific surface area are key points that can dramatically enhance the Li ion storage kinetics by reducing the ion diffusion length and increasing the ion acceptability. Thus, the structural properties of all samples were investigated using FESEM, TEM, and BET analyses.

To determine the crystalline phases of the CoS₂/WS₂-CNF, CoS₂/WS₂-PCNF, and CoS₂/WS₂-HPCNF, their XRD patterns were obtained and analyzed (Fig. 5a). The XRD patterns of all samples show complex peaks of amorphous graphite, CoS₂, and WS₂ phases; the diffraction peak of amorphous graphite is seen at 24.6°, which corresponds to the (002) plane with hexagonal structure [22]; the diffraction peaks of CoS₂ are seen at 32.4°, 39.9°, 54.8°, 57.7°, and 59.9°, corresponding to the (200), (211), (311), (222), and (023) planes, respectively, implying a cubic pyrite-type crystal structure (JCPDS card no. 41–1471) [13]; and the diffraction peaks of WS₂ are seen at 14.5°, 32.8°, 33.7°, 39.7°, 57.6°, and 62.8°, corresponding to the (002), (100), (101), (103), (110), and (107) planes, respectively, implying a hexagonal structure (JCPDS card no. 08–0237) [14]. These results suggest that CoS₂ and WS₂ USP hybrid

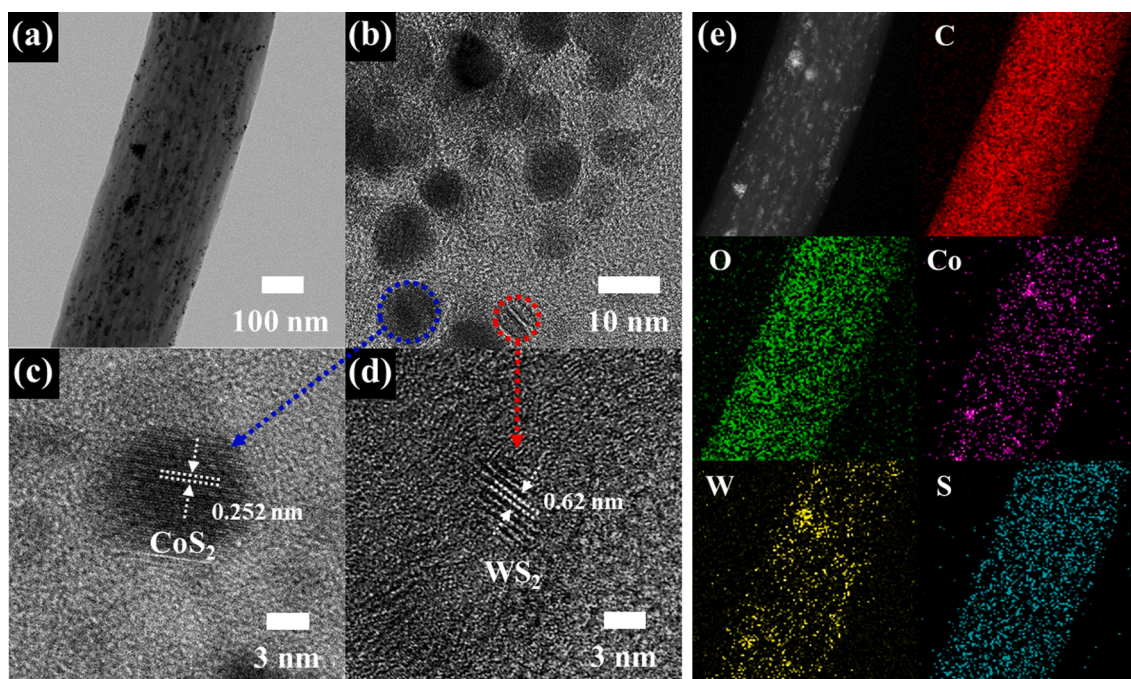


Fig. 3. (a) Low- and (b) high-magnification TEM images, and (c) interlayer distances of CoS₂ and WS₂ USPs in CoS₂/WS₂-HPCNF, respectively. (e) TEM-EDS mapping images indicating C, O, Co, W, and S elements obtained from CoS₂/WS₂-HPCNF.

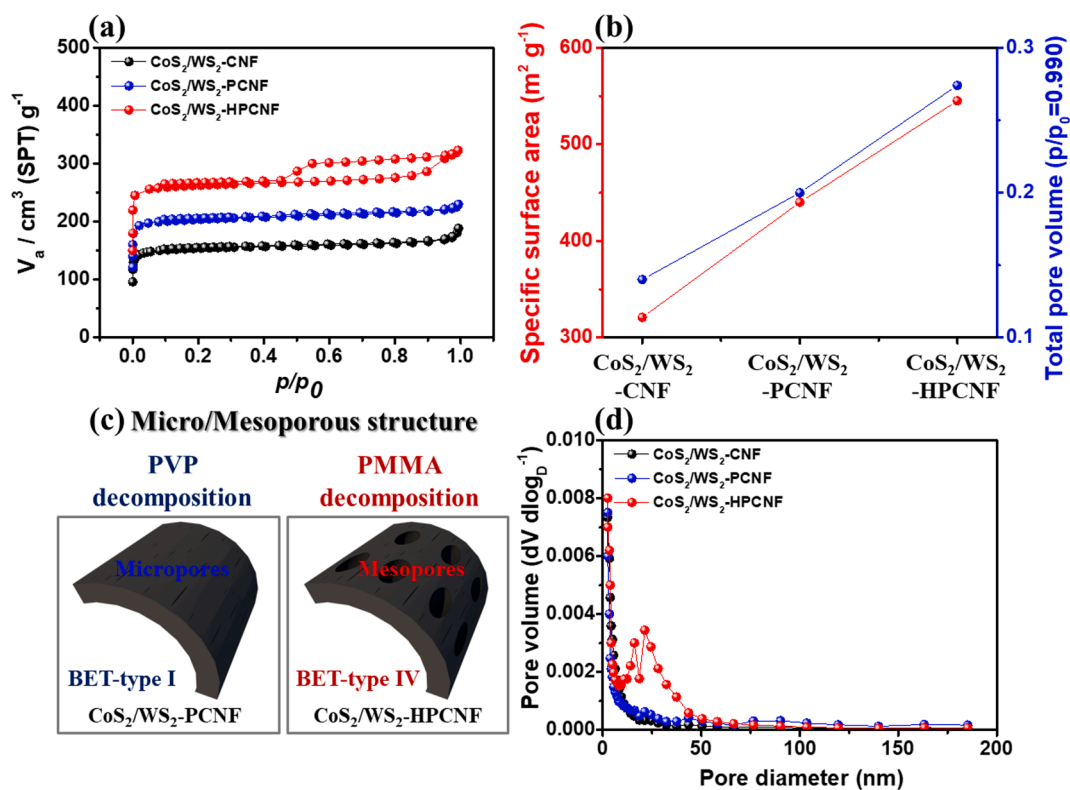


Fig. 4. (a) N_2 adsorption/desorption isotherms curves, (b) graph of specific surface area with total pore volumes of all samples, (c) schematic illustration of pore types, (d) pore size distribution measured at 0.2 to 200 nm of CoS_2/WS_2 -CNF, CoS_2/WS_2 -PCNF, and CoS_2/WS_2 -HPCNF.

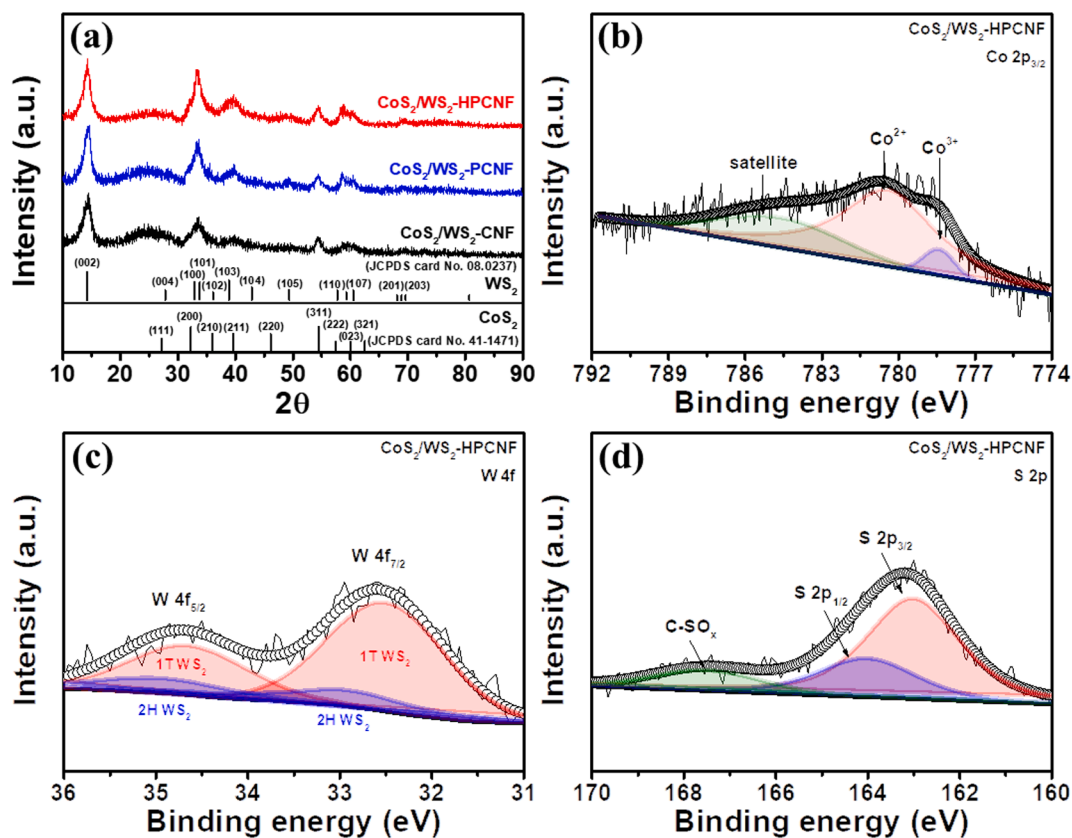


Fig. 5. (a) XRD patterns of CoS_2/WS_2 -CNF, CoS_2/WS_2 -PCNF, and CoS_2/WS_2 -HPCNF. And XPS spectra of (b) Co $2p_{3/2}$, (c) W $4f$, and (d) S $2p$, obtained from CoS_2/WS_2 -HPCNF.

composites were successfully synthesized in the PCNFs during sulfuration. In addition, in the low-angle XRD patterns of all the samples, as shown in Fig. S5, weak diffraction peaks of CoS₂/WS₂-HPCNF can be observed at 0.98°, 1.63°, and 1.87° corresponding to the (100), (110), and (200) planes, respectively, which were induced by some ordered mesopores in the PCNFs [23,24]. This result suggests that mesopores in the CoS₂/WS₂-HPCNF were clearly formed by decomposition of the PMMA polymer. Fig. 5b–d show the XPS spectra of the CoS₂/WS₂-HPCNF, displaying the peaks of Co 2p, W 4f, and S 2p. All XPS spectra were calibrated using the binding energy of 284.5 eV in C 1 s. In the full spectrum of the CoS₂/WS₂-HPCNF, the C 1 s, O 1 s, Co 2p, W 4f, and S 2p peaks are clearly seen without other impurity phases (Fig. S6). Fig. 5b shows the Co 2p_{3/2} spectrum of the CoS₂/WS₂-HPCNF. Here, Co³⁺, Co²⁺, and satellite peaks appeared at ~778.9, ~780.9, and ~784.8 eV, respectively [13]. The Co³⁺ and Co²⁺ peaks correspond to the oxidized-CoS₂ phase and the CoS₂ phase in the PCNFs, respectively. The unit cell of CoS₂ comprises one Co²⁺ ion and six S²⁻ ions, indicating an octahedral structure, and each unit cell is bound by the sharing of vertices (Fig. S7) [13]. Moreover, CoS₂ can lead to an increase in the specific capacity because of its high theoretical capacity (871 mAh g⁻¹) along with good half-metal properties [13]. Fig. 5c shows the W 4f spectrum of the CoS₂/WS₂-HPCNF. Here, two peaks at ~32.6 and ~34.8 eV can be seen, corresponding to W 4f_{7/2} and 4f_{5/2}, respectively [19,20]. The W 4f_{7/2} and W 4f_{5/2} spectra were divided into two areas, one in which major peaks of 1 T-WS₂ (red area) are seen and the other where minor peaks of 2H-WS₂ (blue area) are seen. The WS₂ structure comprises a unit cell, constituting one W²⁺ ion and six S²⁻ ions, which are stacked to form the ABC (1 T-WS₂) or ABA (2H-WS₂) structure (Fig. S8) [19,20]. In particular, the 1 T-WS₂ phase exhibits high electrical/ionic conductivity owing to the metallic properties of the 1 T structure, which can improve the high-rate charge/discharge performance [14,19]. In contrast, 2H-WS₂ exhibits low electrical conductivity due to its large band gap, and thus demonstrates a semiconducting property [14,19]. In particular, the contents of the 1 T-WS₂ and 2H-WS₂ phases were calculated to be 94.7% and 5.3%, respectively, using the W 4f spectrum. Fig. 5d displays the S 2p spectrum of the CoS₂/WS₂-HPCNF. The S 2p spectrum shows three peaks at ~162.9, ~163.8, and ~167.5 eV, corresponding to S 2p_{3/2}, S 2p_{1/2}, and C-SO_x, respectively [13]. The S 2p_{3/2} and S 2p_{1/2} peaks indicate the formation of Co-S and W-S bonds, implying the presence of CoS₂ and WS₂ phases. The C-SO_x state formed by oxidized-S on the PCNF surface during the sulfuration process. Therefore, the CoS₂ and WS₂ phases in the PCNFs were demonstrated via the XRD and XPS analyses.

To further investigate the electrochemical kinetics according to the pore structure of all samples, EIS analyses were performed using fresh cells fabricated by the CoS₂/WS₂-CNF, CoS₂/WS₂-PCNF, and CoS₂/WS₂-HPCNF. Fig. 6a shows the Nyquist plots of all the samples. The Nyquist plots have semi-circular forms in the high-frequency region, followed by lines slanted-upward in the low-frequency region. The semi-circular parts are attributed to the charge transfer resistance (R_{ct}), which is the electrical resistance at the interface between the electrode and the

electrolyte [25,26]. The slanted-line parts are related to the Li ion diffusion impedance in the electrode materials, called the Warburg impedance [27]. In the EIS data, the R_{ct} value and Warburg impedance of the CoS₂/WS₂-HPCNF were significantly lower than those of the CoS₂/WS₂-CNF and CoS₂/WS₂-PCNF. This result suggests that the hierarchical porous structure of the CoS₂/WS₂-HPCNF can effectively provide fast charge transfer kinetics and short ion diffusion length. Furthermore, the Li ion diffusion coefficients could be calculated using the slanted-line parts from the Nyquist plots of all samples in the low-frequency region with the following equations [28]:

$$Z_R = \sigma_w \omega^{-1/2} + R_e + R_{ct} \quad (2)$$

$$D = (RT)^2 / 2A^2 n^4 F^4 C^2 \sigma_w^2 \quad (3)$$

where R_e is the bulk resistance in the cell, involving all components of the electrolyte, separator, and electrode; σ_w is the Warburg impedance coefficient related to the Li ion diffusion resistance; D, R, and T are the Li ion diffusion coefficient, gas constant, and temperature, respectively; and A, n, F, and C are the electrode area, the number of electrons per molecule, Faraday constant, and the concentration of Li ions, respectively. The σ_w values of the CoS₂/WS₂-CNF, CoS₂/WS₂-PCNF, and CoS₂/WS₂-HPCNF were determined as 23.7, 15.6, and 12.0 Ω cm² s^{-1/2}, respectively (Fig. 6b). The D values of all samples were calculated using σ_w. As seen in Fig. 6c, the Li ion diffusion coefficients of the CoS₂/WS₂-CNF, CoS₂/WS₂-PCNF, and CoS₂/WS₂-HPCNF were 0.6 × 10⁻¹², 1.4 × 10⁻¹², and 2.4 × 10⁻¹² cm² s⁻¹, respectively. The increased Li ion diffusion coefficient of the CoS₂/WS₂-HPCNF electrode compared with those of the CoS₂/WS₂-CNF and CoS₂/WS₂-PCNF electrodes, which result from the hierarchical porous structure of the CoS₂ and WS₂ hybrid composites can dramatically improve the ionic diffusion kinetics by short Li ion diffusion length and ion acceptability at high-rate charge/discharge conditions.

Fig. 7a shows the cycling stability performance of all samples measured at the current density of 0.1 A g⁻¹ in the voltage range of 0.05 to 3.0 V up to 100 cycles. For the conventional CNF electrode, the low specific capacity of 282.6 mAh g⁻¹ with the capacity retention of 73.0% remained virtually constant between 20 and 100 cycles (Fig. S9). On the other hand, because of the structural collapse of CoS₂ and WS₂ resulting from extreme volume expansion during cycling, the specific capacities of the commercial CoS₂ and WS₂ electrodes swiftly reduced to 385.5 and 261.1 mAh g⁻¹ with capacity retentions of 51.6% and 39.1% after 100 cycles, respectively (Fig. S10). Therefore, we proposed the introduction of a hierarchical porous structure of a carbon matrix having micropores and mesopores, which can significantly relieve the structural degradation by volume expansion of CoS₂ and WS₂. As a result, the cycling stabilities of the CoS₂/WS₂-CNF, CoS₂/WS₂-PCNF, and CoS₂/WS₂-HPCNF electrodes are improved compared with those of the commercial CoS₂ and WS₂ electrodes. After 100 cycles, the CoS₂/WS₂-CNF electrode exhibited the low specific capacity of 500.8 mAh g⁻¹ with the capacity retention of 72.1% due to a large structural change caused by

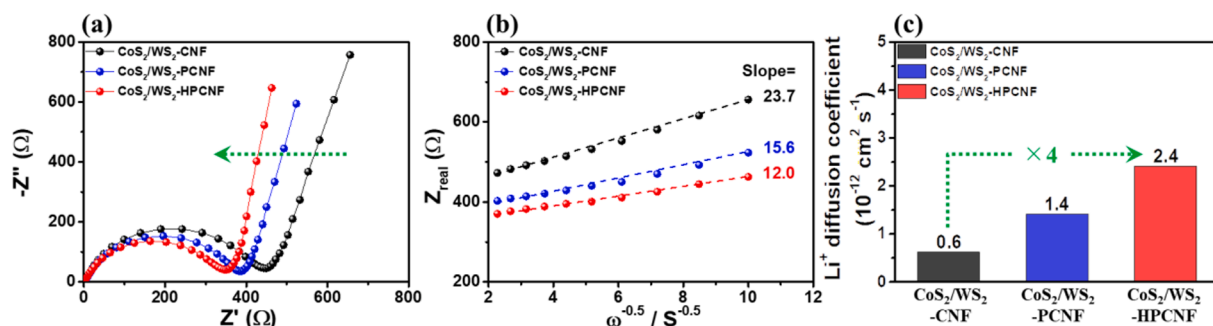


Fig. 6. (a) Nyquist plots, (b) graph of the relationship between Z_{real} and $\omega^{-1/2}$ calculated using inclined line at the low frequency in Nyquist plots, (c) values of Li⁺ diffusion coefficient, obtained from CoS₂/WS₂-CNF, CoS₂/WS₂-PCNF, and CoS₂/WS₂-HPCNF.

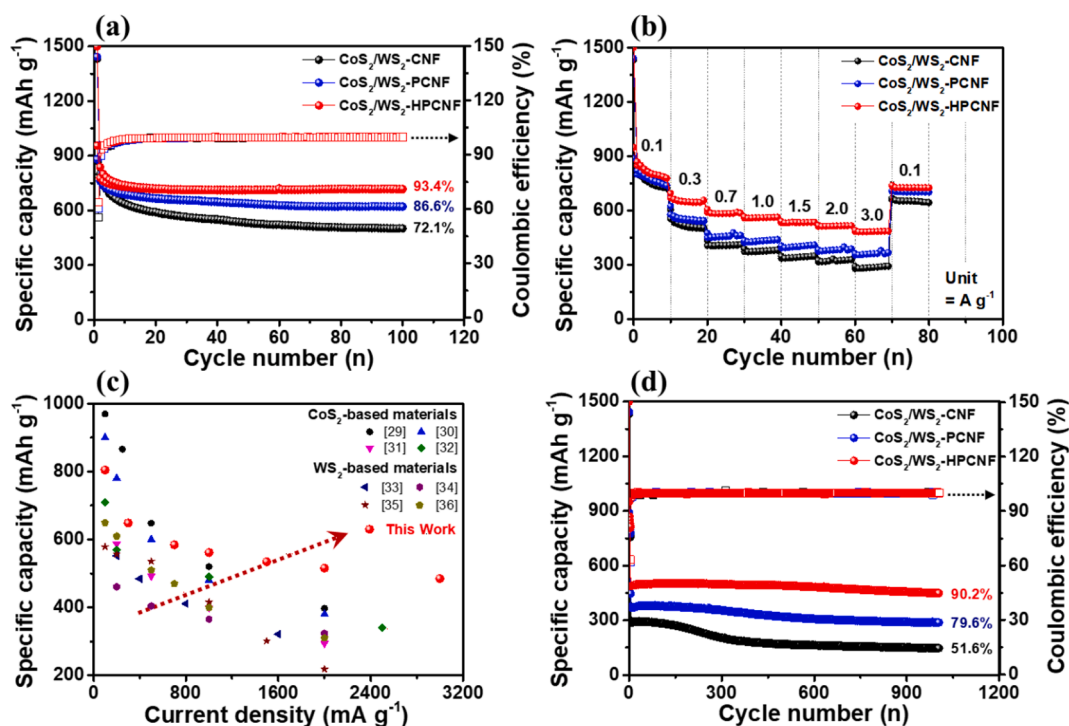


Fig. 7. (a) Cycling stability measurement at current density of 0.1 A g⁻¹ up to 100 cycles, (b) rate capability test at various current densities of 0.1–3.0 A g⁻¹, (c) competition of rate performance measured at various current densities of 0.1–3.0 A g⁻¹ with previously reported CoS₂- and WS₂-based anode materials in LIBs, and (d) ultrafast cycling stability test at 3.0 A g⁻¹ during 1000 cycles.

agglomerated CoS₂ and WS₂ USPs in the CNFs. Nevertheless, the specific capacities of the CoS₂/WS₂-PCNF and CoS₂/WS₂-HPCNF electrodes were 620.6 mAh g⁻¹ and 718.0 mAh g⁻¹ with capacity retentions of 86.6% and 93.4%, respectively, because of the well-dispersed CoS₂ and WS₂ USPs in the PCNFs. These results suggest that the cycling stability of the samples is primarily attributed to the efficient suppression of the volume expansion of the CoS₂ and WS₂ USPs. In addition, the coulombic efficiency of the CoS₂/WS₂-HPCNF electrode is rapidly increased to >99% over five cycles compared with the CoS₂/WS₂-CNF (94.5%) and CoS₂/WS₂-PCNF (96.9%) electrodes due to increased electrical/ionic conductivity. To demonstrate the rate capabilities of the CoS₂/WS₂-CNF, CoS₂/WS₂-PCNF, and CoS₂/WS₂-HPCNF electrodes, their rate performances were measured at the current densities of 0.1, 0.3, 0.7, 1.0, 1.5, 2.0, and 3.0 A g⁻¹ (Fig. 7b). With an increase in the current density from 0.1 to 3.0 A g⁻¹, the specific capacity of the CoS₂/WS₂-CNF electrode rapidly decreased from 775.3 to 283.8 mAh g⁻¹, whereas, those of the CoS₂/WS₂-PCNF and CoS₂/WS₂-HPCNF electrodes were 790.4–357.2 and 840.6–488.4 mAh g⁻¹, respectively. These results suggest that the hierarchical porous structure leads to an improvement in the Li storage kinetics under ultrafast cycling conditions, caused by short diffusion lengths and favorable Li ion acceptability. The capacity retentions and capacity error percentage of all electrodes measured at the current density of 0.1–3.0 A g⁻¹ are shown in Fig. S11 and Table S2. They imply an outstanding rate performance compared with those of previously reported CoS₂- and WS₂-based materials (Fig. 7c) [29–36]. Fig. 7d displays the ultrafast cycling stability test results of the CoS₂/WS₂-CNF, CoS₂/WS₂-PCNF, and CoS₂/WS₂-HPCNF electrodes measured at the current density of 3.0 A g⁻¹ over 1000 cycles. Compared with the CoS₂/WS₂-CNF (291.0 mAh g⁻¹ with capacity retention of 51.6%) and CoS₂/WS₂-PCNF (372.6 mAh g⁻¹ with capacity retention of 79.6%) electrodes, the CoS₂/WS₂-HPCNF electrode exhibited the outstanding fast discharge capacity of 444.5 mAh g⁻¹ with the capacity retention of 90.1% after 1000 cycles. This superior high-rate charge/discharge performance is mainly ascribed to the beneficial Li ion diffusion, which results from the use of a hierarchical porous structure with micropores

and mesopores. Furthermore, after long-term tests at the ultrafast cycling condition of 3.0 A g⁻¹ over 1000 cycles, Nyquist plots of all samples were obtained via EIS analysis (Fig. 8a). The CoS₂/WS₂-CNF electrode showed a sharply increased resistance and poor Warburg impedance owing to the large volume expansion of agglomerated CoS₂ and WS₂ USPs in the CNFs. In contrast, even after the high-rate charge/discharge condition at 3.0 A g⁻¹ over 1000 cycles, the resistance and Warburg impedance of the CoS₂/WS₂-HPCNF remained low because of the effective prevention of volume expansion of CoS₂ and WS₂ USPs as they were well-dispersed in the PCNFs (Fig. 8b). Thus, in the present study, the performance improvement can be ascribed to three main effects (Fig. 9). First, the well-dispersed CoS₂ and WS₂ USPs in the PCNFs provide a high number of Li storage sites, leading to increased specific capacity. Second, the composite structure of carbon with well-dispersed CoS₂/WS₂ USPs efficiently prevents volume expansion related to outstanding cycling stability. Third, the hierarchical porous structure with meso/micropores provides a short Li ion diffusion length and favorable Li ion acceptability, leading to remarkable high-rate charge/discharge performance with fast Li storage kinetics. Therefore, we believe that the CoS₂/WS₂-HPCNF electrode has a prodigious potential as an anode material in ultrafast LIBs.

4. Conclusions

We successfully fabricated well-dispersed CoS₂ and WS₂ USPs embedded into PCNFs (CoS₂/WS₂-HPCNF) with a hierarchical porous structure containing micropores and mesopores; for this purpose, electrospinning, polymer decomposition, and sulfurization were employed. Specifically, we proposed a porous structure of CoS₂ and WS₂ USPs, which can lead to improved high-rate charge/discharge performance. This architecture exhibited an outstanding Li diffusion coefficient (2.4×10^{-12} cm² s⁻¹), which is due to an increase in the number of ion diffusion sites, resulting from a high mesopore volume fraction (38.7%). The improved performance of the CoS₂/WS₂-HPCNF, i.e., high specific capacity of 718.0 mAh g⁻¹ at 0.1 A g⁻¹ after 100 cycles (capacity

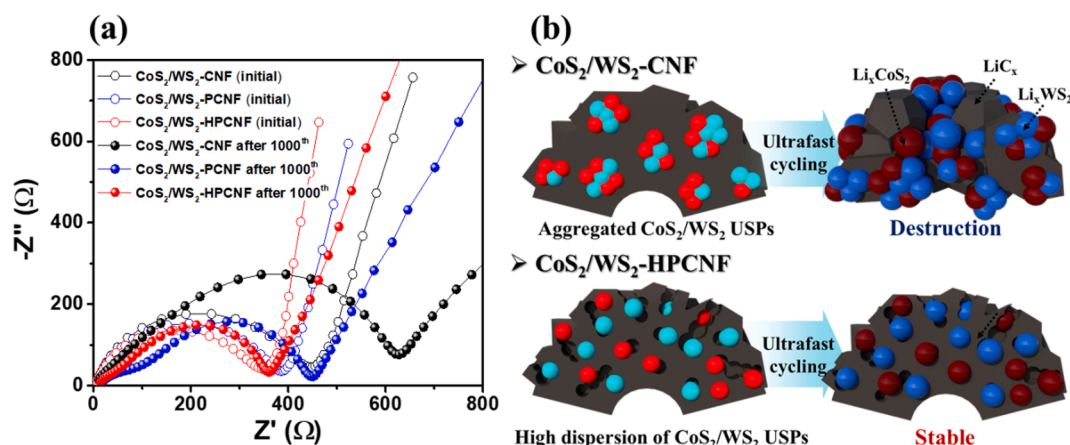


Fig. 8. (a) Nyquist plots of CoS₂/WS₂-CNF, CoS₂/WS₂-PCNF, and CoS₂/WS₂-HPCNF electrodes obtained from initial and after 1000 cycles at current density of 3.0 A g⁻¹. (b) Schematic illustration of destruction mechanism of CoS₂/WS₂-CNF and CoS₂/WS₂-HPCNF.

Novel architecture for ultrafast Li ion batteries

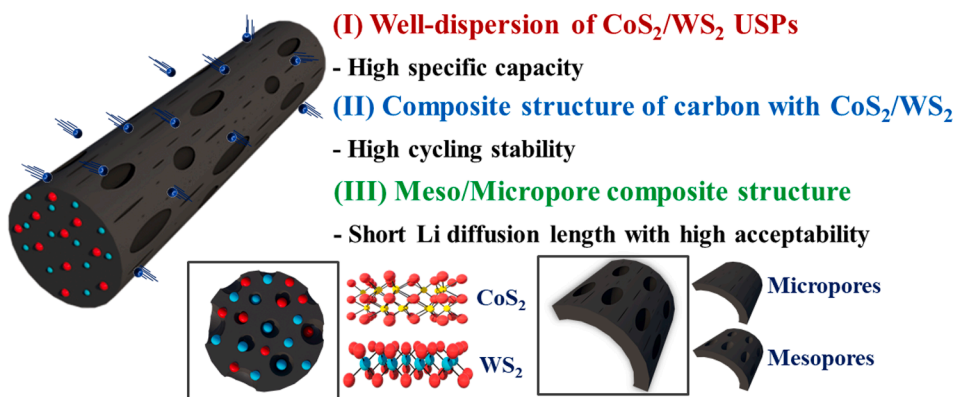


Fig. 9. Schematic illustration of two dominant effects on CoS₂/WS₂-HPCNF for boosting high-rate charge/discharge performances.

retention of 93.4%), outstanding fast discharge capacity of 488.4 mAh g⁻¹ at 3.0 A g⁻¹, and ultrafast cycling stability of 444.5 mAh g⁻¹ at 3.0 A g⁻¹ after 1000 cycles (capacity retention of 90.2%), was attributed to three main factors: (I) the high specific capacity due to well-dispersed CoS₂ and WS₂ USPs embedded into PCNFs, leading to an increase in the number of Li storage sites; (II) the outstanding cycling stability due to the composite structure of carbon with CoS₂/WS₂ USPs, leading to the prevention of volume expansion of CoS₂ and WS₂ USPs; and (III) the remarkable high-rate charge/discharge performance related to the hierarchical porous structure containing micro/mesopores, which can reduce the Li ion diffusion length and enhance the Li ion acceptability. Therefore, these findings indicate that the CoS₂/WS₂ hybrid composite with a hierarchical porous structure is a promising anode material for use in ultrafast LIBs.

CRedit authorship contribution statement

Dong-Yo Shin: Conceptualization, Methodology, Investigation, Writing - original draft. **Jung Soo Lee:** Methodology. **Hyo-Jin Ahn:** Conceptualization, Supervision, Writing - review & editing.

Declaration of Competing Interest

The authors declare that they have no known competing financial interests or personal relationships that could have appeared to influence the work reported in this paper.

Acknowledgement

This work was supported by the National Research Foundation of Korea (NRF) grant funded by the Korea government (MSIT) (No. 2019R1A2C1005836)

Appendix A. Supplementary data

Supplementary data to this article can be found online at <https://doi.org/10.1016/j.apsusc.2021.149298>.

References

- [1] Y. Zhou, M. Su, X. Yu, J.-G. Wang, X. Ren, R. Cao, W. Xu, D.R. Baer, Y. Du, O. Borodin, Y. Wang, X.-L. Wang, K. Xu, Z. Xu, C. Wang, Z. Zhu, Real-time mass spectrometric characterization of the solid-electrolyte interphase of a lithium-ion battery, *Nat. Nanotechnol.* 15 (2020) 224–230.
- [2] G. Mao, W. Wu, Q. Zhou, L. Li, Y. Huang, Y. Yao, D. Chu, H. Tong, X. Guo, Improved electrochemical performance of high-nickel cathode material with electronic conductor RuO₂ as the protecting layer for lithium-ion batteries, *Appl. Surf. Sci.* 531 (2020), 147245.
- [3] P. Benedek, O.K. Forslund, E. Nocerino, N. Yazdani, N. Matsubara, Y. Sassa, F. Juranyi, M. Medarde, M. Telling, M. Mansson, V. Wood, Quantifying Diffusion through Interfaces of Lithium-Ion Battery Active Materials, *ACS Appl. Mater. Interfaces* 12 (2020) 16243–16249.
- [4] Q. Tian, F. Zhang, L. Yang, Fabricating thin two-dimensional hollow tin dioxide/carbon nanocomposite for high-performance lithium-ion battery anode, *Appl. Surf. Sci.* 15 (2019) 1904740.
- [5] Y. Qin, Z. Jiang, L. Guo, J. Huang, Z.-J. Jiang, Controlled thermal oxidation derived Mn₃O₄ encapsulated in nitrogen doped carbon as an anode for lithium/sodium ion batteries with enhanced performance, *Chem. Eng. J.* 406 (2021), 126894.

- [6] S. Lou, Y. Zhao, J. Wang, G. Yin, C. Du, X. Sun, Ti-Based Oxide Anode Materials for Advanced Electrochemical Energy Storage: Lithium/Sodium Ion Batteries and Hybrid Pseudocapacitors, *Small* 11 (2015) 2511–2517.
- [7] S.-J. Lu, Z.-T. Wang, X.-H. Zhang, Z.-J. He, H. Tong, Y.-J. Li, J.-C. Zheng, In Situ-Formed Hollow Cobalt Sulfide Wrapped by Reduced Graphene Oxide as an Anode for High-Performance Lithium-Ion Batteries, *ACS Appl. Mater. Interfaces* 12 (2020) 2671–2678.
- [8] H. Wang, X.K. Qian, H. Wu, R. Zhang, R. Wu, MOF-derived rod-like composites consisting of iron sulfides embedded in nitrogen-rich carbon as high-performance lithium-ion battery anodes, *Appl. Surf. Sci.* 481 (2019) 33–39.
- [9] X. Qian, G. Zhu, K. Wang, F. Zhang, K. Liang, W. Luo, J. Yang, Bowl-like mesoporous polymer-induced interface growth of molybdenum disulfide for stable lithium storage, *Chem. Eng. J.* 381 (2020), 122651.
- [10] J. Ren, R.-P. Ren, Y.-K. Lv, A flexible 3D graphene@CNT@MoS₂ hybrid foam anode for high-performance lithium-ion battery, *Chem. Eng. J.* 353 (2018) 419.
- [11] L. Ma, B. Zhao, X. Wang, J. Yang, X. Zhang, Y. Zhou, J. Chen, MoS₂ nanosheets vertically grown on carbonized corn stalks as lithium-ion battery anode, *ACS Appl. Mater. Interfaces* 10 (2018) 22067.
- [12] X. Lei, K. Yu, R. Qi, Z. Zhu, Fabrication and theoretical investigation of MoS₂-Co₃S₄ hybrid hollow structure as electrode material for lithium-ion batteries and supercapacitors, *Chem. Eng. J.* 347 (2018) 607.
- [13] D.-Y. Shin, H.-G. Jo, H.-J. Ahn, Accelerating lithium storage capability of cobalt sulfide encapsulated within anion dual-doped mesoporous carbon nanofibers, *Appl. Surf. Sci.* 527 (2020), 146895.
- [14] Y.-Y. Yeh, W.-H. Chiang, W.-R. Liu, Synthesis of few-layer WS₂ by jet cavitation as anode material for lithium ion batteries, *J. Alloy. Compd.* 775 (2019) 1251–1258.
- [15] J.S. Lee, J. Jun, S. Cho, W. Kim, J. Jang, Electrospun three-layered polymer nanofiber-based porous carbon nanotubes for high-capacity energy storage, *RSC Adv.* 7 (2017) 201–207.
- [16] J. Lv, W. Gu, X. Cui, S. Dai, B. Zhang, G. Ji, Nanofiber network with adjustable nanostructure controlled by PVP content for an excellent microwave absorption, *Sci. Rep.* 9 (2019) 4271.
- [17] J.L. Payne, J.D. Percival, K. Giagloglou, C.J. Crouch, G.M. Carins, R.I. Smith, R.K. B. Gover, J.T.S. Irvine, In situ thermal battery discharge using CoS₂ as a cathode material, *J. Electrochem. Soc.* 166 (2019) A2660.
- [18] R. Krishnamoorti, Strategies for Dispersing Nanoparticles in Polymers, *MRS Bulletin* 32 (2007) 341–347.
- [19] Y. Hongjian, Y. Yong, L. Jianghao, M. Peiyang, W. Yucheng, Z. Fan, F. Zhengyi, Space-confined growth of Ag₃PO₄ nanoparticles within WS₂ sheets: Ag₃PO₄/WS₂ composites as visible-light-driven photocatalysts for decomposing dyes, *J. Mater. Chem. A* 3 (2015) 19439.
- [20] X. Zhang, H. Xu, J. Wang, X. Ye, W. Lei, M. Xue, H. Tang, C. Li, Synthesis of Ultrathin WS₂ Nanosheets and Their Tribological Properties as Lubricant Additives, *Nanoscale Res. Lett.* 11 (2016) 442.
- [21] D.-Y. Shin, K.-W. Sung, H.-J. Ahn, Synergistic effect of heteroatom-doped activated carbon for ultrafast charge storage kinetics, *Appl. Surf. Sci.* 478 (2019) 499–504.
- [22] D.-Y. Shin, G.-H. An, H.-J. Ahn, Barnacle-like manganese oxide decorated porous carbon nanofibers for high-performance asymmetric supercapacitors, *Ceram. Int.* 44 (2018) 4883–4890.
- [23] X. Wang, Q. Lin, H. Pan, S. Jia, H. Wu, Y. Shi, Z. Wang, Oxidation modification of chitosan-based mesoporous carbon by soft template method and the adsorption and release properties of hydroxycamptothecin, *Sci. Rep.* 10 (2020) 15772.
- [24] J. Wang, Z. Zhang, Q. Zhang, J. Liu, J. Ma, Preparation and adsorption application of carbon nanofiber with large specific surface area, *J. Mater. Sci.* 53 (2018) 16466.
- [25] D.-Y. Shin, D.-H. Park, H.-J. Ahn, Interface modification of an Al current collector for ultrafast lithium-ion batteries, *Appl. Surf. Sci.* 475 (2019) 519–523.
- [26] D.-Y. Shin, K.-W. Sung, H.-J. Ahn, Fluorine-doped carbon quantum dot interfacial layer on stockade-like etched copper foil for boosting Li-ion storage, *Chem. Eng. J.* 31 (2020), 127563.
- [27] D.-Y. Shin, H.-J. Ahn, Interfacial Engineering of a Heteroatom-Doped Graphene Layer on Patterned Aluminum Foil for Ultrafast Lithium Storage Kinetics, *ACS Appl. Mater. Interfaces* 12 (2020) 19210–19217.
- [28] G.-H. An, H. Kim, H.-J. Ahn, Improved Ionic Diffusion through the Mesoporous Carbon Skin on Silicon Nanoparticles Embedded in Carbon for Ultrafast Lithium Storage, *ACS Appl. Mater. Interfaces* 10 (2018) 6235–6244.
- [29] X. Zhang, X.J. Liu, G. Wang, H. Wang, Cobalt disulfide nanoparticles/graphene/carbon nanotubes aerogels with superior performance for lithium and sodium storage, *J. Colloid Interface Sci.* 505 (2017) 23–31.
- [30] Y. Zhang, N. Wang, C. Sun, Z. Lu, P. Xue, B. Tang, Z. Bai, S. Dou, 3D spongy CoS₂ nanoparticles/carbon composite as high-performance anode material for lithium/sodium ion batteries, *Chem. Eng. J.* 332 (2018) 370–376.
- [31] W. Cheng, H. Di, Z. Shi, D. Zhang, Synthesis of ZnS/CoS/CoS₂@N-doped carbon nanoparticles derived from metal-organic frameworks via spray pyrolysis as anode for lithium-ion battery, *J. Alloy. Compd.* 831 (2020), 154607.
- [32] Q. Wang, R. Zou, W. Xia, J. Ma, B. Qiu, A. Mahmood, R. Zhao, Y. Yang, D. Xia, Q. Xu, Facile Synthesis of Ultrasmall CoS₂ Nanoparticles within Thin N-Doped Porous Carbon Shell for High Performance Lithium-Ion Batteries, *Small* 11 (2015) 2511–2517.
- [33] W. Yang, J. Wang, C. Si, Z. Peng, J. Frenzel, G. Eggeler, Z. Zhang, [001] preferentially-oriented 2D tungsten disulfide nanosheets as anode materials for superior lithium storage, *J. Mater. Chem. A* 3 (2015) 17811.
- [34] T. Li, R. Guo, Y. Luo, F. Li, L. Meng, X. Sun, Z. Yang, H. Luo, Y. Wan, Improved lithium and sodium ion storage properties of WS₂ anode with three-layered shell structure, *Electrochim. Acta* 331 (2020), 135424.
- [35] I. Kim, S.-W. Park, D.-W. Kim, Onion-like crystalline WS₂ nanoparticles anchored on graphene sheets as high-performance anode materials for lithium-ion batteries, *Chem. Eng. J.* 375 (2019), 122033.
- [36] Q. Pang, Y. Gao, Y. Zhao, Y.J.H. Qiu, Y. Wei, B. Liu, B. Zou, F. Du, G. Chen, Improved Lithium-Ion and Sodium-Ion Storage Properties from Few-Layered WS₂ Nanosheets Embedded in a Mesoporous CMK-3 Matrix, *Chem.-Eur. J.* 23 (2017) 7074–7080.